



8-20-2014

Oxidation-Resistant, Solution-Processed Plasmonic Ni Nanochain-SiO_x ($x < 2$) Selective Solar Thermal Absorbers

Xiaobai Yu
Dartmouth College

Xiaoxin Wang
Dartmouth College


Qinglin Zhang
University of Kentucky, qinglinzhang@uky.edu

Juchuan Li
Oak Ridge National Laboratory

Jifeng Liu
Dartmouth College, Jifeng.Liu@dartmouth.edu

Right click to open a feedback form in a new tab to let us know how this document benefits you.

Follow this and additional works at: https://uknowledge.uky.edu/cme_facpub

 Part of the [Chemical Engineering Commons](#), and the [Materials Science and Engineering Commons](#)

Repository Citation

Yu, Xiaobai; Wang, Xiaoxin; Zhang, Qinglin; Li, Juchuan; and Liu, Jifeng, "Oxidation-Resistant, Solution-Processed Plasmonic Ni Nanochain-SiO_x ($x < 2$) Selective Solar Thermal Absorbers" (2014). *Chemical and Materials Engineering Faculty Publications*. 8.
https://uknowledge.uky.edu/cme_facpub/8

This Article is brought to you for free and open access by the Chemical and Materials Engineering at UKnowledge. It has been accepted for inclusion in Chemical and Materials Engineering Faculty Publications by an authorized administrator of UKnowledge. For more information, please contact UKnowledge@lsv.uky.edu.

Oxidation-Resistant, Solution-Processed Plasmonic Ni Nanochain-SiO_x (x < 2) Selective Solar Thermal Absorbers

Notes/Citation Information

Published in *Journal of Applied Physics*, v. 116, no. 7, article 073508, p. 1-8.

Copyright 2014 American Institute of Physics. This article may be downloaded for personal use only. Any other use requires prior permission of the author and the American Institute of Physics.

The following article appeared in *Journal of Applied Physics*, v. 116, no. 7, article 073508, p. 1-8 and may be found at <http://dx.doi.org/10.1063/1.4893656>.

Digital Object Identifier (DOI)

<http://dx.doi.org/10.1063/1.4893656>

Oxidation-resistant, solution-processed plasmonic Ni nanochain-SiO_x (x < 2) selective solar thermal absorbers

Xiaobai Yu,¹ Xiaoxin Wang,¹ Qinglin Zhang,² Juchuan Li,³ and Jifeng Liu^{1,a)}

¹Thayer School of Engineering, Dartmouth College, 14 Engineering Drive, Hanover, New Hampshire 03755, USA

²Department of Chemical and Materials Engineering, University of Kentucky, 177 F. Paul Anderson Tower, Lexington, Kentucky 40506, USA

³Materials Science and Technology Division, Oak Ridge National Laboratory, Oak Ridge, Tennessee 37831, USA

(Received 12 July 2014; accepted 10 August 2014; published online 20 August 2014)

Metal oxidation at high temperatures has long been a challenge in cermet solar thermal absorbers, which impedes the development of atmospherically stable, high-temperature, high-performance concentrated solar power (CSP) systems. In this work, we demonstrate solution-processed Ni nanochain-SiO_x (x < 2) and Ni nanochain-SiO₂ selective solar thermal absorbers that exhibit a strong anti-oxidation behavior up to 600 °C in air. The thermal stability is far superior to previously reported Ni nanoparticle-Al₂O₃ selective solar thermal absorbers, which readily oxidize at 450 °C. The SiO_x (x < 2) and SiO₂ matrices are derived from hydrogen silsesquioxane and tetraethyl orthosilicate precursors, respectively, which comprise Si-O cage-like structures and Si-O networks. Fourier transform infrared spectroscopy shows that the dissociation of Si-O cage-like structures and Si-O networks at high temperatures have enabled the formation of new bonds at the Ni/SiO_x interface to passivate the surface of Ni nanoparticles and prevent oxidation. X-ray photoelectron spectroscopy and Raman spectroscopy demonstrate that the excess Si in the SiO_x (x < 2) matrices reacts with Ni nanostructures to form silicides at the interfaces, which further improves the anti-oxidation properties. As a result, Ni-SiO_x (x < 2) systems demonstrate better anti-oxidation performance than Ni-SiO₂ systems. This oxidation-resistant Ni nanochain-SiO_x (x < 2) cermet coating also exhibits excellent high-temperature optical performance, with a high solar absorptance of ~90% and a low emittance ~18% measured at 300 °C. These results open the door towards atmospheric stable, high temperature, high-performance solar selective absorber coatings processed by low-cost solution-chemical methods for future generations of CSP systems. © 2014 AIP Publishing LLC.

[<http://dx.doi.org/10.1063/1.4893656>]

I. INTRODUCTION

Oxidation of metal nanostructures poses a significant challenge in their applications because they have large specific surface area and strong reactivity, leading to easier and faster oxidation than bulk materials. While noble metals are intrinsically resistant to oxidation, they are often too costly for applications in large area coatings. Cermet solar selective absorber coatings for concentrated solar thermal power (CSP) systems^{1,2} are such an example.

CSP and solar photovoltaics (PV) are two major approaches to harvest solar energy. Compared to PV, CSP can be more easily integrated with conventional power plants. In addition, it offers great advantages in low-cost energy storage since the heated working fluid (e.g., molten salt) can be stored and kept at a high temperature for an extended period of time. This is an attractive solution to the intermittency issue of solar energy. Selective solar thermal absorber coatings for CSP systems have been an important research area in solar energy materials.^{1,2} They convert solar energy efficiently into heat with minimal thermal radiation losses in the infrared (IR)

regime. Most of the solar selective absorbers in CSP systems comprise metal nanoparticles embedded in a ceramic matrix, known as “cermet.”^{1–3} Conventionally, the coating is designed as graded refractive index anti-reflection layers in the solar spectrum range, with the volume fraction of the metal nanoparticles gradually increasing from the surface to the coating/substrate interface. The size of metal nanoparticles is in the order of several nm, much smaller the wavelengths of interest. With adequate design of refractive indices profile and thicknesses of the cermet coating layers based on interference effect, low reflectance (high spectral absorptance) in the solar spectral regime and high reflectance (low spectral emittance) in the infrared thermal radiation regime can be achieved simultaneously.^{4–6} There are a couple of disadvantages for the conventional cermet absorbers, though: (1) the thicknesses of the layers need to be precisely controlled for optimal performance, which usually requires more costly vacuum depositions;⁷ (2) The tiny size of the metal nanoparticles makes them highly susceptible to oxidation.⁸ Therefore, most of the CSP receivers have to work under vacuum, which adds to additional cost. Besides, the vacuum breaching also became a major failure mechanism of CSP systems.

To reduce the fabrication cost without sacrificing the performance of the cermet solar absorbers, recently we have

^{a)}Author to whom correspondence should be addressed. E-mail address: Jifeng.Liu@dartmouth.edu. Tel.: +1-603-646-9885; Fax: +1-603-646-8778.

developed solution-processed plasmonic Ni nanochain- Al_2O_3 selective solar thermal absorbers that have achieved a high solar absorptance $>90\%$ and a low thermal emittance $<10\%$ according to the reflectance spectra measured at room temperature.⁹ The spectral selectivity is inherent to the plasmonic response of the Ni nanochains, which can be tuned by their lengths or diameters via solution chemistry. In comparison with the conventional design, the performance of this new nanochain cermet is much less constrained by stringent film thickness requirement, thereby facilitating low-cost solution-based fabrication method. Also, the size of the Ni nanoparticles in the chains is in the order of 100 nm, $\sim 10\times$ larger than those in conventional cermets. The increased size not only leads to plasmonic enhancement of absorption in the solar spectrum regime,⁹ but also makes the nanochains more robust to oxidation.⁸ However, in the Ni nanochain- Al_2O_3 system, Ni nanoparticles are still easily oxidized at $\geq 450^\circ\text{C}$ in air. It has been reported that introducing TiO_2 particles into the Ni-based cermets helped to form compounds with Ni and effectively reduced the oxidation rate, yet the corresponding impact on the optical properties is unknown.¹⁰ In this work, we further develop solution-processed plasmonic Ni nanochain- SiO_x ($x \leq 2$) selective solar thermal absorbers that exhibit a strong oxidation-resistant behavior up to 600°C in air with high optical performance, far superior to the 450°C limitation for Ni nanoparticle- Al_2O_3 selective solar thermal absorbers. These oxidation-resistant cermet coatings will help to alleviate the problem of vacuum breaching failure in CSP systems. This investigation also constitutes an initial step forward towards atmospheric operation of CSP systems.

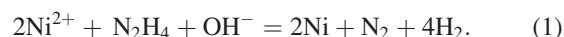
II. EXPERIMENTAL

Considering that metal silicides are much more resistant to oxidation than metals while maintaining the metallic optical properties,^{11,12} we propose to introduce excess Si into the ceramic matrix material. It is expected that the excess Si in the matrix will form silicide-like chemical bonds with the metal nanostructures. The bond energy and bond dissociation energy of Ni-Si are both greater than those of Ni-Ni, indicating that Ni silicides are more chemically stable than Ni against oxidation. Moreover, in the presence of sufficient Si supply, thermodynamics dictates that a SiO_2 layer will preferentially form on the surface of the silicide upon oxidation without affecting the integrity of the silicide itself.^{11,12} Only after the supply of Si is depleted will the silicide oxidation process produce both SiO_2 and metal oxides. Si-rich Ni silicides are even more robust to oxidation than Ni-rich Ni silicides^{11,12} because they have more Si-Si bonds with even higher bond energy than Ni-Si. Therefore, we expect that introducing excess Si into the ceramic matrix material will effectively retard the oxidation process.

Two types of cermet selective solar thermal absorbers have been fabricated in this experiment, i.e., Ni nanochain- SiO_x ($x < 2$) absorbers and Ni nanochain- SiO_2 absorbers. The Ni nanochain- SiO_x ($x < 2$) absorber consists of a thin film with Ni nanochains embedded in a dielectric matrix of SiO_x ($x < 2$). The SiO_x matrix is derived from hydrogen

silsesquioxane (HSQ) diluted by methyl isobutyl ketone (MIBK). Based on the stoichiometry of the HSQ precursor ($\text{H}_8\text{Si}_8\text{O}_{12}$), x is approximately 1.5. The molecular structure of HSQ is shown in Fig. 1.¹³ Under heat treatment at $>700^\circ\text{C}$, the Si-H bonds, the Si-O cage-like structures, and the Si-O networks will start to dissociate,¹⁴ facilitating the formation of new chemical bonds with the Ni nanochains. Since the SiO_x ($x < 2$) is Si-rich, the excess Si could also form silicide-like bonding with Ni nanostructures, as mentioned earlier. To verify the effect of excess Si in the matrix on the oxidation resistance, we also fabricated Ni nanochain- SiO_2 absorber as a comparison. In this case, the nanochains are embedded in a stoichiometric silica matrix derived from tetraethyl orthosilicate (TEOS) using sol-gel method.

Ni nanochains are fabricated by solution-chemical approach. The reaction is



The size of Ni nanoparticles is controlled by $\text{Ni}^{2+}:\text{N}_2\text{H}_4$ ratio, which averages at 80 nm in this case. Besides, the Ni nanoparticles will automatically form Ni nanochains in ethylene glycol solution, which help to enhance the optical performance of the system due to the plasmonic effect in Ni nanochains.⁹ More details about the fabrication process can be found in the supplementary information of Ref. 9. The Ni nanochain suspension and powders are shown in Fig. 2(a). The black color clearly indicates a high spectral absorptance in the visible spectrum regime.

For Ni nanochain- SiO_x ($x < 2$) cermet fabrication, HSQ was diluted with MIBK at a ratio from 1:3 to 1:10 with sonication. The Ni nanochains were mixed with the HSQ/MIBK solution and dispersed uniformly by sonication to form a sol before spin-coating. A scanning electron microscopy (SEM) picture of the Ni nanochain- SiO_x ($x < 2$) cermet is shown in Fig. 2(b).

For Ni nanochain- SiO_2 cermet fabrication, the SiO_2 sol was prepared by mixing TEOS, ethanol, and deionized water with 37.2% wt. HCl acid as catalyst.¹⁵ First, 18 ml TEOS and 12 ml ethanol were mixed with vigorously stirring for 30 min. Then, 10 drops of HCl was introduced to 20 ml deionized water. Next, slowly add the diluted HCl solution into the TEOS-ethanol solution with vigorously stirring at

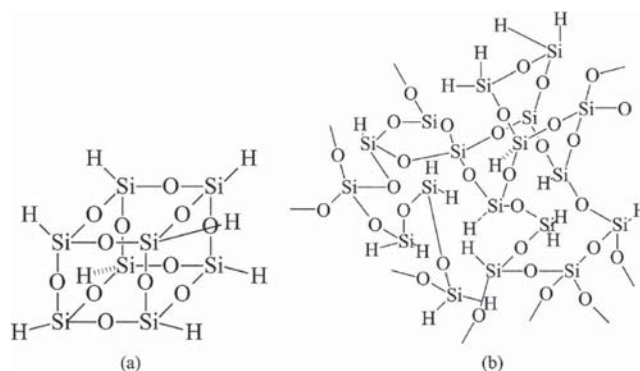


FIG. 1. Chemical structures of HSQ: (a) cage form, (b) network form. Reproduced from C. M. Lampert, *Sol. Energy Mater.* **1**, 319 (1979). Copyright 1979 The Royal Society of Chemistry.

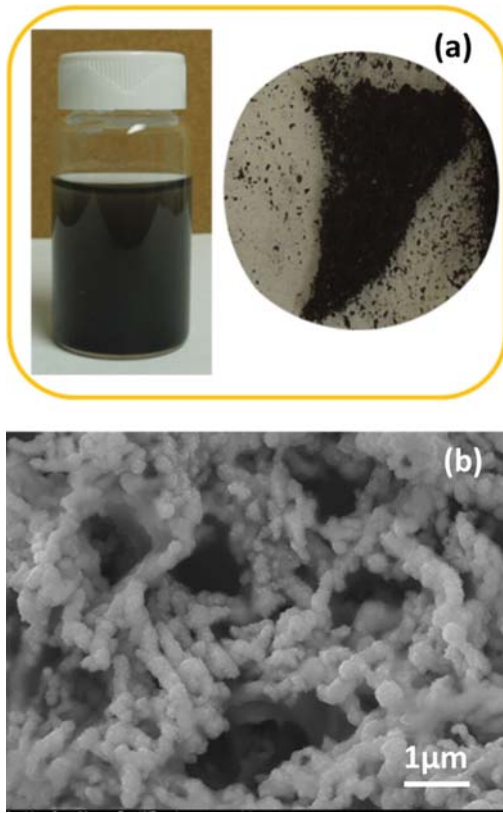


FIG. 2. (a) Photos of Ni nanochain suspension and powders; (b) SEM picture of Ni nanochain-SiO_x ($x < 2$).

60 °C for 2 h. The Ni nanochains were mixed with the as-fabricated TEOS solution and dispersed uniformly by sonication to form a sol before spin-coating.

The two kinds of liquid mixtures were respectively spin-coated on Si or Grade 316 stainless steel (SS) substrates. The dimensions of the substrates were within $2 \times 2 \text{ cm}^2$. The final step was to anneal the sample in a N₂, Ar or reducing atmosphere (e.g., Ar with 5% H₂) at 700–800 °C for 15 to 30 min. Ni nanochain-Al₂O₃ cermet samples were also prepared using the methods described in Ref. 9 for comparison with Ni-SiO_x and Ni-SiO₂ systems. The thickness of all the coatings is controlled to be $\sim 1 \mu\text{m}$.

The anti-oxidation properties of the coated samples were tested in air from 450 °C to 675 °C, and the samples were characterized by X-ray Diffraction (XRD, Cu K α_1 line, $\lambda = 0.15406 \text{ nm}$), X-ray photoelectron spectroscopy (XPS), Raman spectroscopy (excitation laser wavelength $\lambda = 514 \text{ nm}$), and Fourier transform infrared spectroscopy (FTIR) to investigate their crystal structures and chemical bonds. The optical property at room temperature was characterized by measuring the reflectance spectra of the cermet coatings on SS substrates using a UV-VIS-IR spectrometer. An integrating sphere was incorporated into the spectrometer to measure the total reflectance (specular and diffuse) in the wavelength range of $\lambda = 300\text{--}2500 \text{ nm}$. Since the transmittance through the SS substrate is 0, the spectral absorptance, α_λ , can be derived from the reflectance spectra by^{1,2}

$$\alpha_\lambda = 1 - R_\lambda, \quad (2a)$$

where R_λ is the reflectance of the coating at wavelength λ . By integrating α_λ over the AM 1.5 solar spectrum and normalizing it to the incident solar power, we can calculate the overall solar absorptance of the coating^{1,2,9}

$$\alpha_{sol} = \frac{\int I_{sol,\lambda} \alpha_\lambda d\lambda}{\int I_{sol,\lambda} d\lambda} = \frac{\int I_{sol,\lambda} (1 - R_\lambda) d\lambda}{\int I_{sol,\lambda} d\lambda}. \quad (2b)$$

Here, $I_{sol,\lambda}$ is the radiation intensity at wavelength λ in AM 1.5 solar spectrum.

Furthermore, in order to directly characterize the high-temperature emittance of the sample, the emission spectra from the samples at 300 °C are measured and normalized to that of a black body reference sample under the same condition. Note that according to Kirchhoff's law, at each wavelength λ , the spectral absorptance is equal to the spectral emittance under thermal equilibrium, i.e., $\alpha_\lambda = \varepsilon_\lambda$. Therefore, by measuring the spectral emittance at 300 °C, we can also obtain the corresponding solar absorptance using Eq. (2b). The overall thermal emittance at 300 °C can be derived as^{1,2,9}

$$\varepsilon_{therm} = \frac{\int I_{black,\lambda} \varepsilon_\lambda d\lambda}{\int I_{black,\lambda} d\lambda}. \quad (2c)$$

Here, $I_{black,\lambda}$ is the 300 °C black body radiation intensity at wavelength λ .

III. RESULTS AND DISCUSSION

A. Anti-oxidation behavior

Fig. 3 shows the XRD data of Ni nanochain-SiO_x ($x < 2$) coated on Si substrate before and after annealing in N₂ at 750 °C for 20 min. A bump around 25° can be clearly seen for the Ni nanochain-SiO_x ($x < 2$) sample before annealing compared to the data after annealing, which corresponds to the amorphous HSQ matrix. This bump disappears after annealing since the Si-O cages and network in HSQ dissociate, as will be discussed in more detail in Sec. III B. The two peaks at 44.5° and 51.8° correspond to Ni (111) and Ni (200), respectively. No Ni oxide peaks are found.

The Ni nanochain-SiO_x ($x < 2$) sample and a Ni nanochain-Al₂O₃ reference sample were then annealed at 450 °C

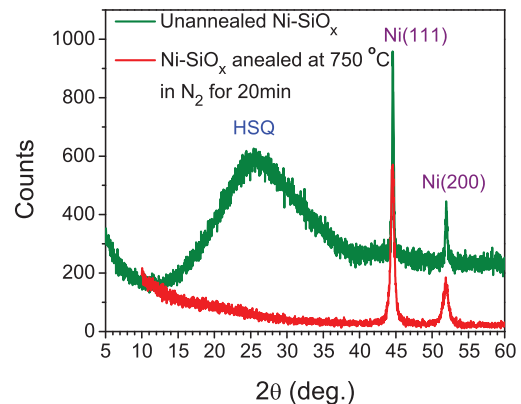


FIG. 3. XRD data of Ni nanochain-SiO_x ($x < 2$) cermet coatings on Si substrate before and after annealing in N₂ at 750 °C for 20 min.

in air for various durations and characterized by XRD each time to test their anti-oxidation properties. Fig. 4(a) shows the XRD results of both samples after 15 min's annealing in air. It is very clear that strong NiO peaks (especially compared to the Ni peaks) show up in the Ni nanochain- Al_2O_3 XRD pattern, while the Ni nanochain- SiO_x ($x < 2$) XRD pattern only shows very little NiO signals. Since neither Raman nor transmission electron microscopy (TEM) analysis identify any NiO in amorphous state, we can conclude that all NiO formed in the samples are crystalline. This is not surprising since the NiO formation can be considered as inserting O atoms into the octahedral interstitials of Ni's face-centered cubic (FCC) lattice. Therefore, we can use the XRD peak intensity of NiO vs. Ni to determine the extent of oxidation. The result in Fig. 4(a) indicates that during the first 15 min's annealing in air, the Ni nanoparticles are much better protected from oxidation in the Ni nanochain- SiO_x ($x < 2$) system compared to the Ni nanochain- Al_2O_3 system. Fig. 4(b) further shows the XRD data of the Ni nanochain- SiO_x ($x < 2$) coating on SS substrates annealed at 500 °C in air. The XRD pattern shows almost no change when the annealing time is increased from 20 min to 90 min, indicating that the oxidation is effectively retarded at this temperature. The results in Figs. 3 and 4 also indicate that the oxidation-resistant behavior of the Ni nanochain- SiO_x ($x < 2$) cermet coating is independent of the substrate.

For each XRD pattern, the intensity ratio of NiO (200) to Ni (111) was calculated to characterize the extent of oxidation because they are the strongest peaks in NiO and Ni,

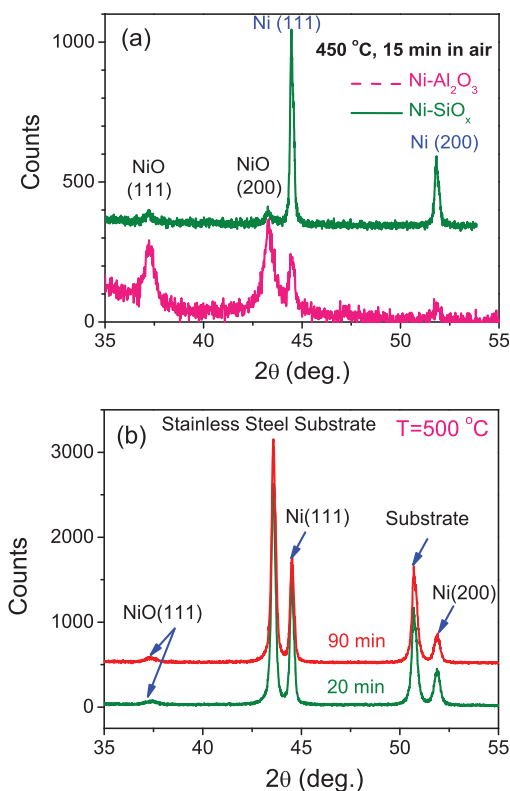


FIG. 4. XRD data of (a) Ni nanochain- SiO_x (on Si) and Ni nanochain- Al_2O_3 coatings annealed in air at 450 °C for 15 min; (b) Ni nanochain- SiO_x coating on stainless steel substrate annealed in air at 500 °C for 20 min and 90 min.

respectively. This helps to reduce the effect of measurement errors on the quantitative analysis of the oxidation process. Fig. 5 compares the NiO/Ni XRD peak ratios of the Ni nanochain- SiO_x ($x < 2$) samples, the Ni nanochain- SiO_2 samples, and the Ni nanochain- Al_2O_3 samples annealed at 450–600 °C in air for up to 2 h. Note that the vertical axis is in log scale in order to show all the data in the same plot. Clearly, the extent of oxidation in Ni- SiO_x ($x < 2$) and Ni- SiO_2 systems are 1–2 orders of magnitude lower than the Ni- Al_2O_3 system when annealed in air at 450 °C. In fact, even after annealing at 600 °C in air, the NiO/Ni XRD peak ratio of the Ni- SiO_x system is still an order of magnitude lower than the Ni- Al_2O_3 system annealed at 450 °C. Compared to Ni- SiO_2 system, Ni- SiO_x ($x < 2$) system is more resistant to oxidation, as indicated by 3–4 \times lower NiO/Ni XRD peak ratio under the same annealing conditions. These results demonstrate that both the SiO_2 matrix itself and the excess Si in the matrix contribute to the anti-oxidation behavior. The mechanism will be discussed in more detail in Sec. III B.

To analyze the oxide growth mechanism in Ni- SiO_x system at 450–600 °C, we applied Deal–Grove model¹⁶ to fit the relation between the extent of oxidation and annealing time, as shown by the dashed lines in Fig. 6. According to the model, the reaction-limited oxidation increases linearly with time, while the diffusion-limited oxidation follows the square-root law, as described in Eq. (2)

$$r_{\text{NiO/Ni}} = At + B\sqrt{t}. \quad (3)$$

Here, $r_{\text{NiO/Ni}}$ is the NiO(200)/Ni(111) XRD peak ratio, t is the annealing time, and A and B are the fitting parameters. This model fits the data at 450 and 550 °C very well. For both cases, the parameter A is negligibly small compared to B . Therefore, the oxidation processes at both temperatures are dominated by diffusion. On the other hand, the model does not fit the data at 600 °C very well, especially considering that the NiO/Ni ratio does not change between 80 and 120 min of annealing. As a comparison, the solid black curve shows another fitting using an phenomenological exponential association model to capture the saturation after long-time annealing and the reaction limited linear oxidation as $t \sim 0$

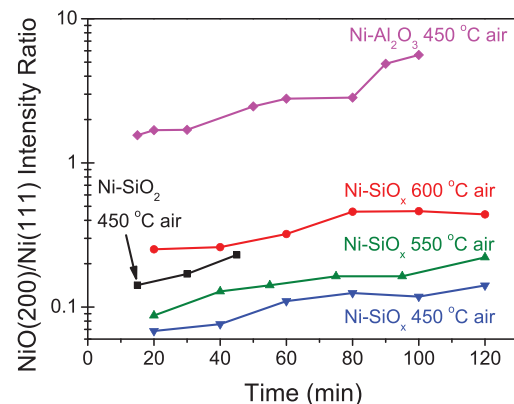


FIG. 5. NiO(200)/Ni(111) XRD peak intensity ratio vs. annealing time at different temperatures (450–600 °C) for Ni- SiO_x , Ni- SiO_2 , and Ni- Al_2O_3 systems. The extent of oxidation in Ni- SiO_x is nearly 2 orders less than Ni- Al_2O_3 , and 3–4 \times less than the Ni- SiO_2 system at 450 °C. Note: the vertical axis is in log scale.

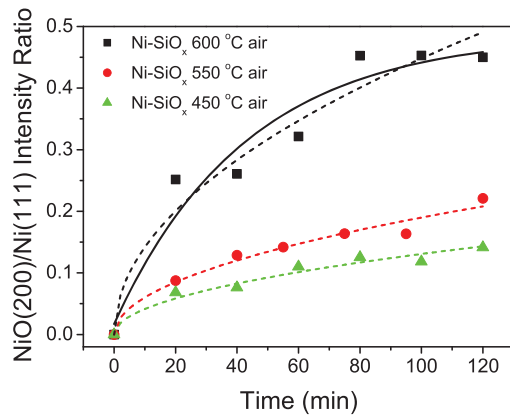


FIG. 6. NiO(200)/Ni(111) XRD peak ratio vs. annealing time in Ni-SiO_x ($x < 2$) system at 450, 550, and 600 °C in air. The dashed lines show the fitting curves using Deal-Grove oxidation model. The solid line shows a fitting curve using phenomenological exponential association model for the case of 600 °C annealing.

$$r_{\text{NiO/Ni}} = A(1 - e^{-Bt}). \quad (4)$$

This fitting works better at $t > 60$ min, but the overall coefficient of determination (R^2) is similar to the Deal-Grove model. As we will discuss in Sec. III B, this complication is likely due to the interfacial silicide phase transformation from Ni₃Si towards NiSi₂ at ≥ 600 °C, which significantly slows down the oxidation rate.

In order to further investigate the effect of thermal activation on the oxidation mechanism, we annealed the same Ni nanochain-SiO_x ($x < 2$) sample in air from 450 up to 675 °C. At each temperature, the sample was annealed for 40 min. After each annealing, we performed XRD analysis to determine the intensity ratio of NiO(200):Ni(111). Further employing quantitative X-ray diffraction analyses¹⁷ that take into account the volume of the unit cells and the structure, multiplicity, Lorentz-polarization (LP), and thermal factors^{18,19} listed in Table I, we can obtain the NiO molar fraction after each annealing from these intensity ratios. After deriving the amount of oxide growth upon each annealing, we calculated the activation energy E_a of oxidation using an Arrhenius plot, as shown in Fig. 7. In the temperature range of 500–600 °C, an activation energy of $E_a = 0.95 \pm 0.19$ eV is derived. This is comparable to the bonding energy of Ni-Si dimers (0.745 eV)²⁰ as well as the activation energy for oxidation of silicides,¹¹ implying the possibility of nickel silicide formation in the Ni-SiO_x ($x < 2$) system.

TABLE I. Parameters used in quantitative XRD analysis.

	Structure ^a	Multiplicity	LP ^b	Thermal ^c
Ni(111)	$ 4f_{\text{Ni}} ^2$	8	11.37	0.96
NiO(200)	$ 4f_{\text{Ni}^{2+}} + 4f_{\text{O}^{2-}} ^2$	6	12.06	1.00

^aThe atomic form factors at the given X-ray wavelength (0.15406 nm) and diffraction angles θ are: $f_{\text{Ni}} = 19.1$, $f_{\text{Ni}^{2+}} = 19.3$, and $f_{\text{O}^{2-}} = 4.8$.¹⁷

^bThe Lorentz-polarization factor is $(1 + \cos^2 2\theta) / (\sin^2 \theta \cos \theta)$.

^cThe thermal factors (also known as Debye-Waller factors) for Ni and NiO are calculated using the parameters in Refs 18 and 19, respectively.

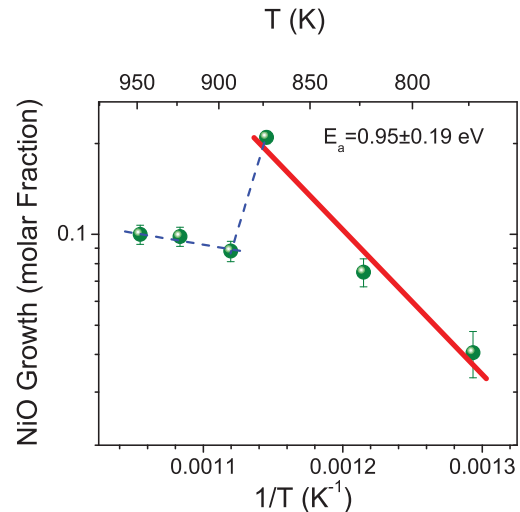


FIG. 7. Arrhenius plot of NiO growth in Ni-SiO_x system from 450 °C to 675 °C. An Arrhenius fitting is given in the temperature range of 450–600 °C with an oxidation activation energy of $E_a = 0.95 \pm 0.19$ eV. The NiO growth rate slows down dramatically at > 600 °C due to silicide phase transformation at the Ni/SiO_x interface, as will be discussed in Sec. III B.

A remarkable feature in Fig. 7 is that the oxidation process deviates significantly from the Arrhenius plot at > 600 °C, indicating that other mechanisms start to play a role. As we will discuss in Sec. III B, this phenomenon is likely due to the silicide phase transformation at > 600 °C, which leads to more Si-rich silicides that are more robust to oxidation. The oxidation kinetics is slowed down correspondingly.

B. Chemical bonding analysis

To understand the interfacial atomic bonds between the Ni nanostructures and the matrix that lead to the anti-oxidation behavior in Ni-SiO_x ($x < 2$) system, we performed FTIR, XPS, and Raman spectroscopy analysis to probe the change in the chemical bonding upon annealing.

Fig. 8 shows the FTIR spectra of the Si substrate (reference), the unannealed HSQ, the Ni-SiO_x ($x < 2$) sample annealed at 750 °C in N₂, and the Ni-SiO_x ($x < 2$) sample

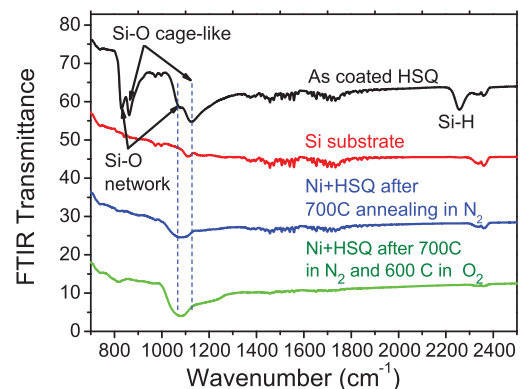


FIG. 8. FTIR spectra of (1) unannealed HSQ on Si substrate (black line); (2) Si substrate alone (red line); (3) Ni nanochain-SiO_x ($x < 2$) on Si annealed in N₂ at 750 °C (blue line); and (4) Ni nanochain-SiO_x ($x < 2$) on Si annealed in N₂ at 750 °C followed by 600 °C in air (green line).

annealed at 750 °C in N₂ followed by 600 °C annealing in air. As mentioned earlier, the structure of HSQ has two forms: Si-O-Si cage and Si-O-Si network (see Fig. 1).¹³ The associated vibration modes of the Si-O-Si network and cage structures are at 1070 cm⁻¹ and 1130 cm⁻¹, while the bending modes are at 830 and 880 cm⁻¹, respectively.^{21,22} When mixed with Ni and annealed at around 750 °C, the intensity of vibration modes at 1070 cm⁻¹ and 1130 cm⁻¹ both decrease, with the latter one (cage structure) decreasing more significantly. The bending modes cannot be observed any more after the annealing, consistent with the observation in Ref. 21. The FTIR spectrum does not show a significant change after further annealing in air at 600 °C. These results indicate the dissociation of the cage and network structures in the SiO_x (x < 2) matrix. During this process, the Ni nanostructures could form new chemical bonds with Si, Si-O network, and/or Si-O-Si cage in the SiO_x (x < 2) matrix, which help to resist oxidation at high temperatures in air. Similar mechanism may also apply to the Ni-SiO₂ system derived from TEOS precursor, which also has Si-O network structures. Compared to stoichiometric SiO₂, SiO_x (x < 2) has excess Si that may also form silicide-like bonding with Ni, thereby adding more protection to the Ni nanostructures. To verify this assumption, XPS and micro-Raman analyses were applied to probe the Ni-Si bonds in the Ni-SiO_x (x < 2) system.

Fig. 9 shows the XPS data of the Ni-SiO_x samples. As expected, signals from various Ni silicides were obtained. For the Ni 2p spectra, the unannealed Ni-SiO_x (x < 2) and Ni-SiO_x (x < 2) annealed in N₂ showed peaks at similar positions, which correspond to Ni 2p_{3/2} (852.7 eV), Ni₃Si 2p_{3/2} (852.8 eV), and Ni₃Si 2p_{1/2} (870.0 eV).^{23,24} Selected area electron diffraction studies (not shown here) also confirmed the formation of Ni₃Si in the sample annealed in N₂ at 750 °C. For the sample annealed in N₂ at 750 °C followed by annealing in air at 675 °C, NiSi₂ 2p_{3/2} (854.6 eV), 2p_{1/2} (871.8 eV) and its satellite peak (880 eV) are clearly observed, along with the NiO 2P_{3/2} and its satellite peaks at 855 and 861 eV, respectively. From these observations, it can be concluded that Ni-rich Ni silicides (Ni₃Si) were formed on the surfaces of Ni nanoparticles through the

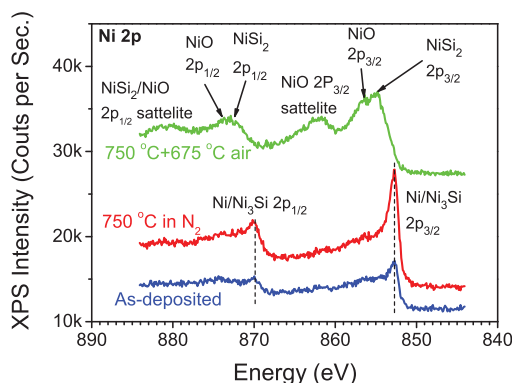
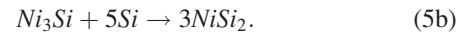
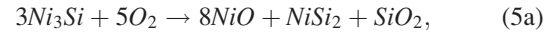


FIG. 9. XPS spectra of (1) unannealed Ni-SiO_x (x < 2) on Si (blue line); (2) Ni-SiO_x (x < 2) on Si annealed in N₂ at 750 °C (red line); and (3) Ni-SiO_x (x < 2) on Si annealed in N₂ at 750 °C and then in air up to 675 °C (green line). Silicide formation is clearly observed after annealing.

process of mixing and annealing in N₂. After being annealed in air at >600 °C, Ni₃Si further reacts with oxygen and/or the excess Si in the matrix and transforms into a Si-rich silicide phase (i.e., NiSi₂) and NiO. For instance, chemical reactions like Eqs. (5a) and (5b) could occur during this air annealing process



Note that NiSi₂ is more resistant to oxidation than Ni₃Si since it is more Si-rich. It has been shown that NiSi₂ can sustain an accelerated oxidation test at 850 °C in steam for 20 min without any measurable oxidation.¹¹ Therefore, after the formation of NiSi₂ at ≥600 °C, the oxidation kinetics is significantly slowed down. This silicide phase transformation explains the sudden decrease in oxidation rate at ≥600 °C shown in Fig. 7, as well as the saturation of oxidation after annealing for >80 min at 600 °C in Fig. 6.

The Raman spectroscopy of the Ni-SiO_x sample annealed at 750 °C in N₂ followed by 675 °C in air further confirms the Si-rich silicide formation. As shown in Fig. 10, NiSi and NiSi₂ Raman peaks were found at 224, 292, 332, and 404 cm⁻¹, which are largely consistent with 216, 288, 320, and 397 cm⁻¹ observed in previous research.^{25,26} We notice that the peaks generally shift to larger wavenumbers compared to literature, which may indicate compressive strain in these silicide interfacial layers. Due to equipment cut-off at <190 cm⁻¹, we are unable to observe Ni₃Si and Ni₂Si Raman peaks at <190 cm⁻¹.²⁷ Overall, the Raman and XPS data indicate that multiple silicide phases, including Ni₃Si, NiSi, and NiSi₂ are formed at the Ni/matrix interface to protect the Ni nanostructures from oxidation.

C. Optical properties at room temperature and high temperature

To characterize the optical properties of our anti-oxidation cermet coatings, Ni nanochain-SiO_x cermets are spin-coated on SS substrates. As mentioned in Sec. II, the reflectance spectra (R_λ) of the samples have been measured at room temperature using an integrating sphere in the UV-VIS-IR spectrometer to capture both specular and

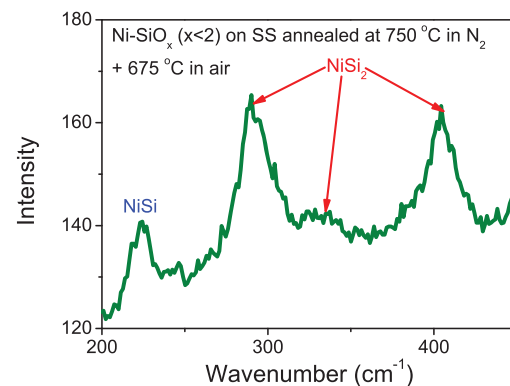


FIG. 10. Raman spectrum of Ni-SiO_x (x < 2) on stainless steel substrate annealed at 750 °C in N₂ followed by 675 °C in air. Peaks corresponding to NiSi and NiSi₂ are clearly observed.

diffuse reflectance in all directions. The corresponding spectral absorptance/emittance data of $\alpha_\lambda = \varepsilon_\lambda = 1 - R_\lambda$ are shown in Fig. 11(a). Curves 1–3 respectively correspond to the data for the SS substrate only, the Ni-SiO_x ($x < 2$) coating on SS before being annealed in air, and Ni-SiO_x ($x < 2$) on SS after being annealed in air at 450 °C for 4 h. As shown in curve 1, the α_λ of the SS substrate is only around 30%–40% in the visible regime. It is expected that the selective solar thermal absorber will significantly increase the spectral absorptance in the visible regime while maintaining a low spectral emittance in the infrared regime. Sure enough, the Ni nanochain-SiO_x cermet coatings increase α_λ in the UV, visible, and near infrared regime to $\sim 90\%$ ($\lambda = 300\text{--}850\text{ nm}$), as shown in curves 2 and 3. Furthermore, we find that after 4 h annealing at 450 °C in air (curve 3), an even lower ε_λ in the infrared regime is achieved without notably sacrificing the high α_λ in the visible regime

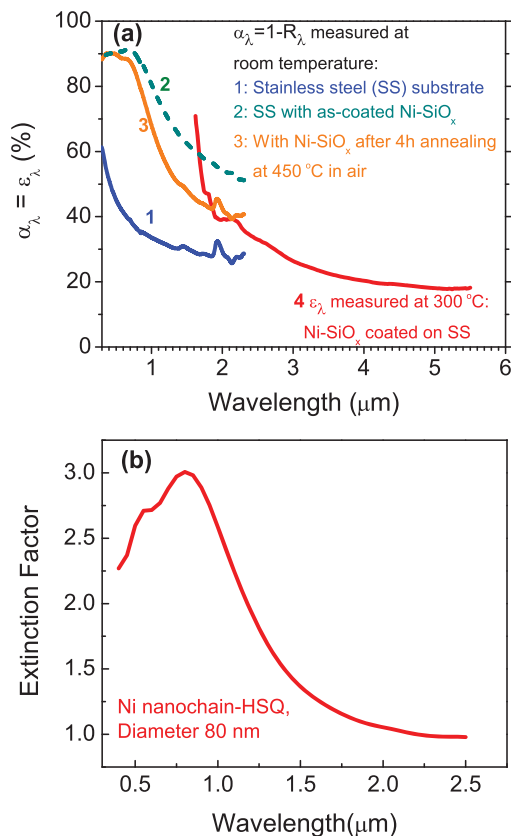


FIG. 11. (a) Spectral absorptance/emittance ($\alpha_\lambda = \varepsilon_\lambda$) derived from room-temperature reflectance spectra using Eq. (2a) (curves 1–3) and directly measured emission spectra at 300 °C (curve 4). Curve 1: SS substrate alone; curve 2: as-coated Ni nanochain-SiO_x on SS substrate; Curve 3: Ni nanochain-SiO_x on SS substrate annealed in air at 450 °C for 4 h; and curve 4: spectral emittance ε_λ measured at 300 °C for Ni nanochain-SiO_x on SS substrate previously annealed in air at 450 °C for 4 h. The emission spectrum from the sample at 300 °C is measured and normalized to that of a black body reference sample under the same condition. The data show a significant red-shift in the spectral absorptance/emittance edge from $\lambda \sim 1.0$ to $\lambda \sim 1.8\ \mu\text{m}$ compared to room temperature, covering almost the entire solar spectrum regime. (b) Theoretically calculated optical response of Ni nanochain-SiO_x ($x < 2$) at room temperature using the methods in Ref. 9. The extinction factor refers to the extinction cross-section divided by the cross-section of the Ni nanoparticles, and it is proportional to the absorption coefficient.

compared to the unannealed one (curve 2). This result directly confirms the effectiveness of the anti-oxidation Ni nanochain-SiO_x selective solar absorber coating. Using the dielectric functions of Ni and HSQ at room temperature and the finite element method described in Ref. 9, the theoretically calculated optical response is shown in Fig. 11(b). The theoretically modelled optical extinction factor, defined as the extinction cross-section divided by the cross-section of the Ni nanoparticles, starts to decrease at $\lambda > 1.0\ \mu\text{m}$. This is consistent with the roll-offs in the α_λ spectra at $\lambda > 1.0\ \mu\text{m}$ in curves 2 and 3 of Fig. 11(a), considering that the extinction factor is proportional to the absorption coefficient at a given wavelength λ . Note that this roll-off wavelength ($\lambda_{\text{roll-off}} \sim 1.0\ \mu\text{m}$) is shorter than that of the Ni nanochain-Al₂O₃ system reported in Ref. 9 ($\lambda_{\text{roll-off}} \sim 2.3\ \mu\text{m}$) although the sizes of the Ni nanoparticles are the same. This shift in $\lambda_{\text{roll-off}}$ is due to the higher refractive index of Al₂O₃ compared to HSQ (1.7 vs. 1.4). Such a spectral shift with the matrix refractive index is a typical feature of surface plasma response.²⁸ The magnitude of the extinction factor before the roll-off, on the other hand, is similar to the case of Al₂O₃, since it is mainly determined by the dielectric function of Ni itself instead of the matrix. From curves 2–3 in Fig. 11(a) and Eq. (2b), we can also derive that the overall solar absorptance α_{sol} for the Ni nanochain-SiO_x cermet coatings are 83% and 78% before and after annealing in air at 450 °C for 4 h, respectively. The major limiting factor of the solar absorptance is that the spectral absorptance rolls off a relatively short wavelength of $\lambda_{\text{roll-off}} \sim 1.0\ \mu\text{m}$. If the spectral absorptance edge can be red-shifted to $\sim 2\ \mu\text{m}$, the absorption will cover almost the entire solar spectrum and α_{sol} will increase correspondingly. One should also keep in mind that the plasmonic response spectrum may redshift at elevated operation temperatures due to the increase of matrix refractive index with temperature. Therefore, it is interesting to directly measure the spectral emittance/absorptance at high temperatures.

As mentioned in Sec. II, the spectral emittance $\varepsilon_\lambda (= \alpha_\lambda)$ at 300 °C (Fig. 11(a), curve 4) is characterized by directly measuring the emission spectrum from the Ni nanochain-SiO_x sample previously annealed in air at 450 °C for 4 h and normalizing the spectrum to that of the black body reference. Note that at this temperature, the thermal emission at $\lambda < 1.5\ \mu\text{m}$ is too weak to measure directly, so the curve starts at $\lambda = 1.6\ \mu\text{m}$. Compared to the result at room temperature, the optical performance at 300 °C is even better since the edge of the $\alpha_\lambda (= \varepsilon_\lambda)$ spectra is indeed notably red-shifted from $\lambda = 1.0\ \mu\text{m}$ (room temperature) to $\sim 1.8\ \mu\text{m}$, covering almost the entire solar spectral regime. Considering that the thermal expansion of Ni is in the order of 10^{-3} at 300 °C, its electron density and corresponding contribution to dielectric function hardly changes compared to that of the room temperature. Therefore, the red-shift is most likely due to the change in the refractive index of the cermet matrix as the temperature increases to 300 °C. On the other hand, the magnitude of the extinction factor before the roll-off is insensitive to the refractive index change of the matrix, as discussed earlier in comparing the optical response of the Ni-SiO_x system with the Ni-Al₂O₃ system. Thus, we expect that α_λ at

$\lambda < 1.4 \mu\text{m}$ for 300°C is $\sim 90\%$, similar to the value before the roll-off in curve 3. Further applying Eq. (2b), it is estimated that the overall solar absorptance α_{sol} at 300°C is $\sim 89\%$ based on the redshift in spectral absorptance/emittance. The thermal emittance ε_{therm} at 300°C is calculated to be 18% using Eq. (2c), assuming that the spectral emittance levels at 0.17 for $\lambda > 5.5 \mu\text{m}$. Such an assumption is supported by the theoretical analyses in Fig. 11(b) and in Ref. 9, which show that the extinction factor slowly decreases with the increase of wavelength after the roll-off. Therefore, the coating exhibits excellent spectral performance in high-temperature operation. This result also suggests that the high-temperature dielectric function of the SiO_x ($x < 2$) matrix derived from HSQ needs to be investigated in order to further optimize the design and performance of the Ni-nanochain cermet coating at high working temperatures.

IV. CONCLUSIONS

In this work, oxidation-resistant Ni nanochain- SiO_x ($x < 2$) selective solar absorber coatings have been fabricated by a vacuum-free, low-cost solution-chemical method for CSP applications. Compared to Ni- Al_2O_3 system which is readily oxidized at 450°C in air, the Ni nanochain- SiO_x ($x < 2$) system exhibits a strong anti-oxidation behavior up to 600°C in air. There are two major factors contributing to the anti-oxidation behavior: (1) the dissociation of Si-O cage-like structures and Si-O networks in the SiO_x ($x < 2$) matrix at high temperatures enables the formation of new bonds at the Ni/ SiO_x interface to passivate the surface of Ni nanoparticles and prevent oxidation; (2) the excess Si in the SiO_x ($x < 2$) matrices reacts with Ni nanostructures to form silicides at the interface, which further improves the anti-oxidation properties. This anti-oxidation Ni nanochain- SiO_x coating also demonstrates excellent high-temperature optical performance, with a high solar absorptance $\sim 90\%$ and a low thermal emittance $\sim 18\%$ at 300°C even after previous annealing in air at 450°C for 4 h. These results represent an initial step forwards towards atmospherically stable, high temperature, high-performance solar selective absorber coatings processed by low-cost solution chemical methods for future generations of CSP systems. The silicide enhanced anti-oxidation mechanism can be readily extended to other metal nanoparticle systems.

ACKNOWLEDGMENTS

This work has been supported by National Science Foundation (NSF) Small Business Innovation Research

(SBIR) Program under the contract number 1315245 via the subcontract from Norwich Technologies, Inc. We would also like to thank Ms. Veronika Stelmakh and Dr. Jay Senkevich at MIT and Mr. Emil Cashin at Norwich Technologies for their help with the high-temperature emittance measurements.

- ¹J. A. Duffie and W. A. Beckman, *Solar Engineering of Thermal Processes*, 3rd ed. (John Wiley & Sons, 2006).
- ²C. E. Kennedy, "Review of mid- to high temperature solar selective absorber materials," National Renewable Energy Laboratory (NREL) Report, Washington, DC, 2002.
- ³C. M. Lampert, *Sol. Energy Mater.* **1**, 319 (1979).
- ⁴P. Spinelli, M. Hebbink, R. de Waele, L. Black, F. Lenzmann, and A. Polman, *Nano Lett.* **11**, 1760 (2011).
- ⁵F. Cao, K. McEnaney, G. Chen, and Z. Ren, "A review of cermet-based spectrally selective solar absorbers," *Energy Environ. Sci.* **7**, 1615 (2014).
- ⁶T. Bostrom, E. Wackelgard, and G. Westin, *Sol. Energy* **74**, 497 (2003).
- ⁷N. Selvakumar and H. C. Barshilia, *Sol. Energ. Mater. Sol. Cells* **98**, 1 (2012).
- ⁸P. A. Chernavskii, N. V. Peskov, A. V. Mugtasimov, and V. V. Lunin, *Russ. J. Phys. Chem. B* **1**, 394 (2007).
- ⁹X. X. Wang, H. F. Li, X. B. Yu, X. L. Shi, and J. F. Liu, *Appl. Phys. Lett.* **101**, 203109 (2012).
- ¹⁰M. A. Farrokhzad and T. I. Khan, *Oxid. Met.* **81**, 267 (2014).
- ¹¹W. J. Strydom, J. C. Lombaard, and R. Pretorius, *Thin Solid Films* **131**, 215 (1985).
- ¹²J. P. Gambino and E. G. Colgan, *Mater. Chem. Phys.* **52**, 99 (1998).
- ¹³C. C. Yang and W. C. Chen, *J. Mater. Chem.* **12**, 1138 (2002).
- ¹⁴C. M. Hessel, E. J. Henderson, and J. G. C. Veinot, *Chem. Mater.* **18**, 6139 (2006).
- ¹⁵A. Gungor, H. Demirtas, I. Atilgan, and M. Yasar, in *Proceedings of the International Iron and Steel*, Karabuk, Turkey, April, 2012, pp. 694–699.
- ¹⁶B. E. Deal and A. S. Grove, *J. Appl. Phys.* **36**, 3770 (1965).
- ¹⁷Y. Waseda, E. Matsubara, and K. Shinoda, *X-ray Diffraction Crystallography*, 1st ed. (Springer, 2011).
- ¹⁸C. G. Windsor and R. N. Sinclair, *Acta Cryst. A* **32**, 395 (1976).
- ¹⁹A. Corrias, G. Mountjoy, G. Piccaluga, and S. Solinas, *J. Phys. Chem. B* **103**, 10081 (1999).
- ²⁰A. N. Andriotis, M. Menon, G. E. Froudakis, Z. Fthenakis, and J. E. Lowther, *Chem. Phys. Lett.* **292**, 487 (1998).
- ²¹A. A. Kumbhar, S. K. Singh, and R. O. Dusane, *Thin Solid Films* **501**, 329 (2006).
- ²²T. S. Chang, T.-C. Chang, P.-T. Liu, T.-S. Chang, and F.-S. Yeh, *Thin Solid Films* **498**, 70 (2006).
- ²³Y. Cao, L. Nyborg, and U. Jelvestam, *Surf. Interface Anal.* **41**, 471 (2009).
- ²⁴M. A. Peck and M. A. Langell, *Chem. Mater.* **24**, 4483 (2012).
- ²⁵S. K. Donthu, D. Z. Chi, S. Tripathy, A. S. W. Wong, and S. J. Chua, "Micro-Raman spectroscopic investigation of NiSi films formed on BF_4^- , B^+ - and non-implanted (100) Si substrates," *Appl. Phys. A* **79**, 637 (2004).
- ²⁶F. F. Zhao, S. Y. Chen, Z. X. Shen, X. S. Gao, J. Z. Zheng, A. K. See, and L. H. Chan, *J. Vac. Sci. Technol. B* **21**, 862 (2003).
- ²⁷P. S. Lee, D. Manginck, K. L. Pey, Z. X. Shen, J. Ding, T. Osipowicz, and A. See, *Electrochem. Solid State Lett.* **3**, 153 (2000).
- ²⁸H. Raether, *Surface Plasmon on Smooth and Rough Surface and Gratings* (Springer-Verlag, Berlin, 1986).